



## PHOCUS radiometer

O. Nyström<sup>1</sup>, D. Murtagh<sup>2</sup>, and V. Belitsky<sup>1</sup>

<sup>1</sup>Group for Advanced Receiver Development, Department of Earth and Space Sciences, Chalmers University of Technology, Gothenburg, Sweden

<sup>2</sup>Global Environmental Measurements and Modelling, Department of Earth and Space Sciences, Chalmers University of Technology, Gothenburg, Sweden

Correspondence to: O. Nyström (olle.nystrom@gmail.se)

Received: 5 December 2011 – Published in Atmos. Meas. Tech. Discuss.: 10 January 2012

Revised: 8 May 2012 – Accepted: 16 May 2012 – Published: 15 June 2012

**Abstract.** PHOCUS – Particles, Hydrogen and Oxygen Chemistry in the Upper Summer Mesosphere is a Swedish sounding rocket experiment, launched in July 2011, with the main goal of investigating the upper atmosphere in the altitude range 50–110 km. This paper describes the SondRad instrument in the PHOCUS payload, a radiometer comprising two frequency channels (183 GHz and 557 GHz) aimed at exploring the water vapour concentration distribution in connection with the appearance of noctilucent (night shining) clouds. The design of the radiometer system has been done in a collaboration between Omnisys Instruments AB and the Group for Advanced Receiver Development (GARD) at Chalmers University of Technology where Omnisys was responsible for the overall design, implementation, and verification of the radiometers and backend, whereas GARD was responsible for the radiometer optics and calibration systems.

The SondRad instrument covers the water absorption lines at 183 GHz and 557 GHz. The 183 GHz channel is a side-looking radiometer, while the 557 GHz radiometer is placed along the rocket axis looking in the forward direction. Both channels employ sub-harmonically pumped Schottky mixers and Fast Fourier Transform Spectrometers (FFTS) backends with 67 kHz resolution.

The radiometers include novel calibration systems specifically adjusted for use with each frequency channel. The 183 GHz channel employs a continuous wave CW pilot signal calibrating the entire receiving chain, while the intermediate frequency chain (the IF-chain) of the 557 GHz channel is calibrated by injecting a signal from a reference noise source through a directional coupler.

The instrument collected complete spectra for both the 183 GHz and the 557 GHz with 300 Hz data rate for the

183 GHz channel and 10 Hz data rate for the 557 GHz channel for about 60 s reaching the apogee of the flight trajectory and 100 s after that. With lossless data compression using variable resolution over the spectrum, the data set was reduced to  $2 \times 12$  MByte.

The first results indicate that the instrument successfully performed measurements of the mesospheric water profile as planned. However, the temperature environment for the instruments showed more extreme behaviour than expected and accounted for. Consequently, the results of the calibration and the final data reduction will need careful treatment. Further, simulations through finite element method (FEM), modelling and direct measurements of the simulated thermal environment and its impact on the instrument performance are described, as well as suggestions for improvements in the design for future flights.

### 1 Introduction

The polar summer mesosphere is an area of intense research, as reflected by the large number of workshops and conference sessions dedicated to the processes occurring there and by the launch in 2007 of NASA's AIM satellite (National Aeronautics and Space Administration, 2012). Phenomena such as noctilucent clouds are regarded as an important test bench for our understanding of interactions in the middle atmosphere and, in the long run, for climate variability in this region.

Noctilucent clouds (NLC) and polar mesosphere summer echoes (PMSE) are two phenomena related to ice particles in the polar summer mesopause region (Thomas, 1991; Rapp

and Lübken, 2004). Existing just at the edge of feasibility, mesospheric ice clouds are expected to be extremely sensitive to changes in middle atmospheric conditions. Consequently, it has been argued that even small long-term changes of mesospheric water vapour (e.g. due to anthropogenic methane emissions or changes in lower atmospheric circulation patterns) or mesospheric temperatures (e.g. due to anthropogenic carbon dioxide emissions) could lead to prominent long-term changes of the observed properties of mesospheric ice clouds (Thomas et al., 1989). The question of whether such long-term changes are already evident in the experimental record has been debated (Thomas et al., 2003; Zahn, 2003). In addition, the occurrence of mesospheric ice particles has also been discussed in connection with satellite launcher exhaust (Stevens et al., 2003, 2005), the observed differences between the Arctic and Antarctic mesosphere (Hervig and Siskind, 2005) and the coupling between the Northern and Southern Hemispheres as observed in the middle atmosphere (Becker and Fritts, 2006). Observations of NLC are an important tool for studies of all these interactions. However, in order to draw robust conclusions from such observations, we need a similarly robust understanding of the relevant physical and chemical processes that govern the properties of mesospheric ice clouds (Rapp and Thomas, 2006).

The properties of mesospheric particle layers and their relationship to various phenomena are among the most challenging questions in current middle atmospheric research. Important topics concern the relationship between meteoric smoke and ice, ice particle nucleation and evolution, and the possible influence of these particle species on gas-phase chemistry. To study these questions the PHOCUS (Particles, Hydrogen and Oxygen Chemistry in the Upper Summer Mesosphere) rocket project was devised. This paper concerns only the water vapour instrument that was designed to allow quasi in-situ measurements as part of a larger package covering meteoric smoke, the light scattering properties of the NLC particles, and chemical composition (Gumbel, 2007).

The specific task of the water vapour experiment is to determine to what extent water vapour is redistributed in altitude by the forming, sedimentation and subsequent sublimation of the NLC particles. The LIMA model has suggested that there could be a narrow layer of water vapour just below the NLC layer with a considerable mixing ratio. This has not so far been clearly detected by satellite instruments.

### 1.1 Requirements

The most important requirement is to obtain significantly better vertical resolution than the satellite measurements (5–10 km) on the order of 1 km, in addition to being a near local measurement. A rocket-born instrument can fulfil these requirements providing that the signal-to-noise ratio is sufficiently high that short integration times can be used. Water vapour measurements from a rocket vehicle have been

made previously using an optical technique by Khaplanov et al. (1996). Such a method is however not possible to use during the sunlit conditions prevailing in the summer mesopause region. Croskey (Croskey et al., 1993) first suggested using passive microwave measurements, but the technology at the time would have required cryogenic temperatures and accurate control of the rocket attitude to obtain the desired signal-to-noise performance. Improved technology allowed us to avoid the extra complexity and expense of altitude control at the expense of reduced observation time with maximum signal.

### 1.2 Rocket flight specifics

The specific rocket vehicle chosen for the PHOCUS payload was a Nike-improved Orion combination subjecting the payload to considerable shock and vibration. In flight the rocket rotates at a rate of  $4 \text{ rev s}^{-1}$  and travels at more than  $1 \text{ km s}^{-1}$  through the height region of interest. These conditions require a robust instrument and short integration times.

## 2 The instrument

### 2.1 Technical description

SondRad comprises two radiometers covering the water absorption lines at 183.31 GHz and 556.936 GHz. The 183 GHz receiver is side-looking and is placed in the middle section of the rocket (Fig. 1). The 557 GHz receiver, pointing parallel to the rocket axis, is placed approximately two meters above, in the nose cone section. Both radiometers employ sub-harmonically pumped Schottky mixers, where the 183 GHz mixer is provided by RPG (Radiometric Physics GmbH, 2011) and the 557 GHz mixer is provided by VDI (Virginia Diodes Inc., 2011). The local oscillator (LO) sources for both radiometers employ active multiplier chains at 85 GHz and 91 GHz. The LOs were developed by Omnisys Instruments AB (Omnisys Instruments AB, 2011). The active 85 GHz multiplier pumps the 183 GHz mixer directly, whereas the 91 GHz chain is followed by a power amplifier with x3 multiplier stage that sub-harmonically pumps the 557 GHz mixer. The FFT-spectrometer backend, provided by Omnisys Instruments AB, processes a 275 MHz band with 4096 channels (Ekebrand, 2011).

The two radiometers employ two different calibration techniques described in more detail in the Sect. 2.2. The 183 GHz receiver utilizes a pilot signal for calibration, whereas calibration of the 557 GHz receiver is implemented by the use of a broadband calibrated noise source. Pictures and a block diagram of the complete system are shown in Figs. 1 and 2. On the rocket, the 557 GHz radiometer is located in the top “particle module” and the 183 GHz radiometer is located in the “side photometer module” (Fig. 1). The backend, with the FFT spectrometer and the control unit, is placed on the same platform as the 183 GHz receiver.

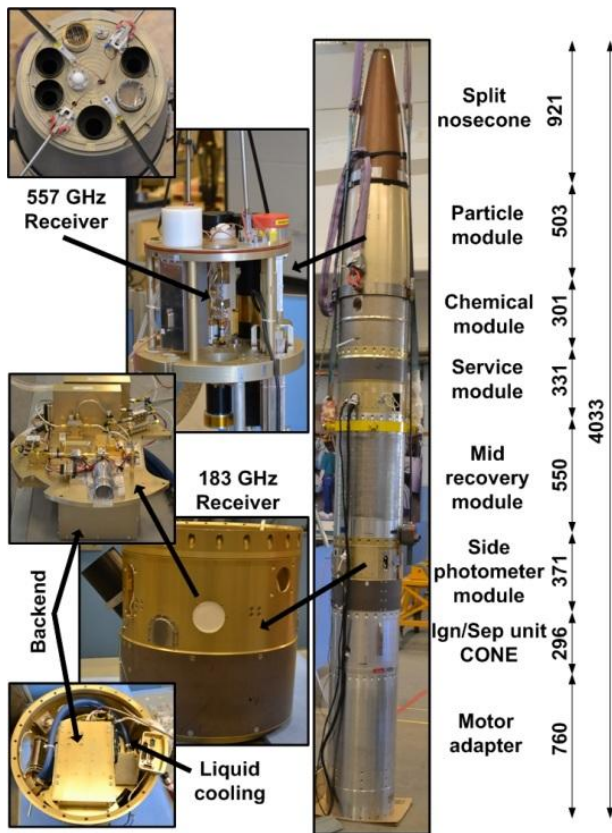


Fig. 1. Pictures of the 557 GHz and the 183 GHz radiometers taken during the rocket assembly at Esrange, Kiruna, and their respective placement on the rocket. All lengths are in mm.

The observation period started at 40 km altitude for the 183 GHz radiometer and at nose cone ejection (approx. 60 km) for the 557 GHz radiometer. The observation period continues until approximately 100 s into the return trajectory. During the observation time, the instrument collected data with 300 Hz sampling rate for the 183 GHz receiver and 10 Hz for the 557 GHz receiver. For the 183 GHz radiometer, channel 183.310 GHz ± 19.3 MHz was recorded from the FFT backend data and in addition 182.264 GHz ± 0.5 MHz, for the calibration signal. For the 557 GHz radiometer, the channel 556.936 GHz ± 19.3 MHz was recorded from the FFT backend data. The reason for limiting the spectral width is to reduce the amount of data stored. Initially, the data are stored locally in SDRAM, with limited capacity, and are dumped to non-volatile data storage at the apogee, as well as after the return to an observation stop altitude. A further step to reduce the amount of data is to vary the spectral bandwidth of the channels by keeping a high resolution, 67 kHz, at the centre of the band and decrease the resolution by combining channels towards the band edges. By doing this, the number of channels is reduced from 576 to 184. With lossless data compression using the variable resolution

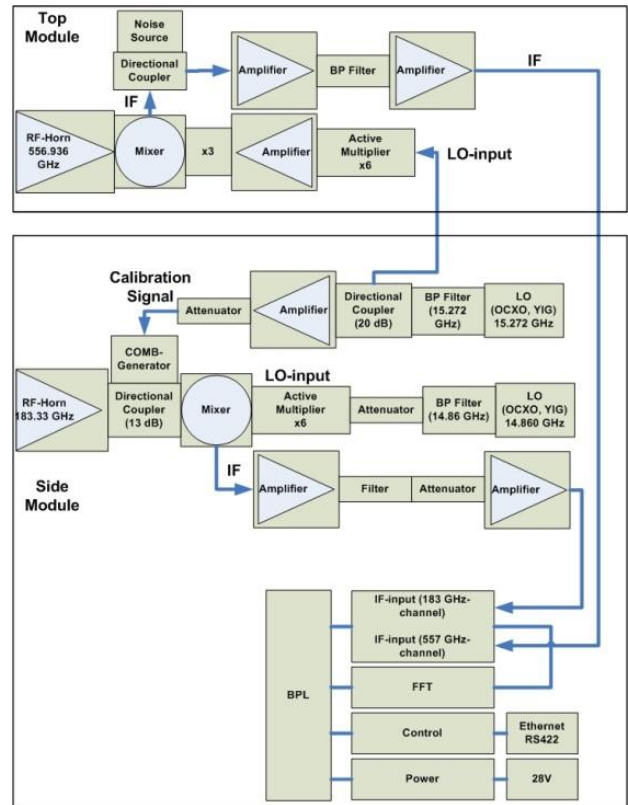


Fig. 2. Layout of the top and side modules. The backend is located in the side module.

over the spectrum, the recorded data set is reduced to approximately 0.12 MByte s<sup>-1</sup> observation. As mentioned above, the tasks of building the backend and housekeeping the computing system for data handling were done by Omnisys Instruments AB.

## 2.2 Measurement accuracy and calibration

A typical application for a radiometer in atmospheric or radio astronomical observation is to detect very weak signals, buried in noise. If the system noise is completely uncorrelated, i.e. white noise, signal integration over time will reduce the noise according to the radiometric equation (Rohlf and Wilson, 2000):

$$\sigma = \frac{T_{\text{System}}}{\sqrt{B\tau}} \quad (1)$$

where  $T_{\text{system}}$  is the total system noise ( $T_{\text{antenna}} + T_{\text{receiver}}$ ),  $B$  is the detection bandwidth,  $\tau$  is the integration time, and  $\sigma$  is the resulting standard deviation. In reality, the noise in a radiometer is a combination of white noise, the DC (Direct Current) drift, and 1/f noise. The DC drift and 1/f noise limit the possibility of reducing the noise by integration, and an optimum integration time can be calculated by the Allan variance (Allan, 1966). This means that further integration will

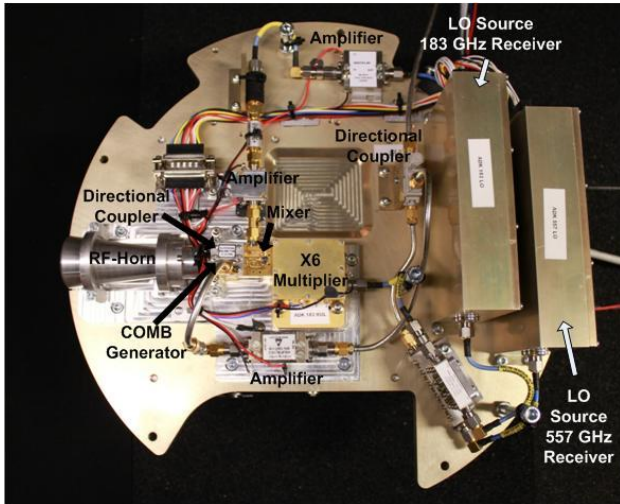


**Fig. 3.** Picture of the 183 GHz side module containing the radiometer, calibration system, and LOs for the 183 GHz and 557 GHz receivers. The backend is located on the back side of the radiometer base plate.

not improve the signal-to-noise ratio. Apart from the noise-originated instability of the receiver, the gain of the receiver varies over time. This can, for instance, vary if the physical temperature of the receiver changes, and it implies that a calibration of the receiver is needed in order to be able to compensate for the gain drift over the entire observation period. The time periods between calibration sequences should be well within the characteristic time of the gain instability.

The most common calibration technique for radiometers is the use of a Dicke-switch (Dicke, 1946), where the reference signals are radiation from a black body at two different and specific, accurately known, temperatures,  $P_{\text{Hot}}/P_{\text{Cold}}$ . The received power can be calculated according to Planck's black body radiation law in the Rayleigh-Jeans limit (Rohlf's and Wilson, 2000), and, assuming a perfectly matched single-mode waveguide, the received power can be calculated as

$$P = k_B B T \quad (2)$$

where  $k_B$  is the Boltzmann's constant,  $B$  is the detection bandwidth, and  $T$  is the brightness temperature of the black body. The receiver noise temperature is then calculated according to a well-known relation:

$$T_e = \frac{T_{\text{Hot}} - Y \cdot T_{\text{Cold}}}{Y - 1} \quad (3)$$

where  $Y$  is the ratio  $P_{\text{Hot}}/P_{\text{Cold}}$ , i.e. the IF output power of the radiometer when exposed to the different loads. This technique calibrates the entire receiver chain (optics, mixer, and low-noise amplifiers, LNAs) and is usually implemented by employing a opto-mechanical switch (e.g. a chopper wheel or

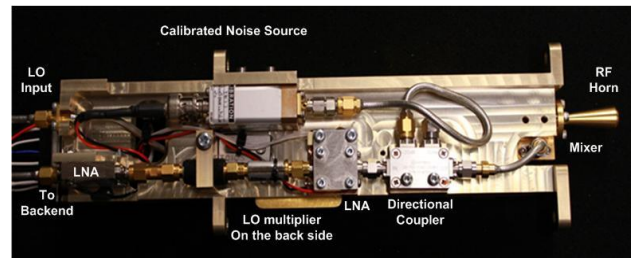


**Fig. 4.** Picture of the 557 GHz radiometer with the horn, noise source, coupler, and LNAs. The mixer and LO-multiplier are located on the other back side.

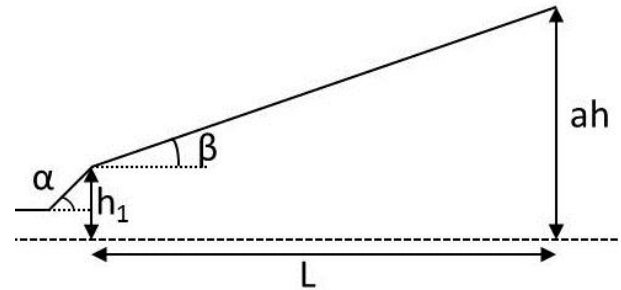


**Fig. 5.** Horn profile of the horns with a flared step, defined by  $\alpha$  and  $h_1$ , generating higher order modes.

a mechanical switch placed in the receiver input beam). Another common problem of the standard Dicke-switch calibration technique is that no measurements can be performed during the calibration cycle; hence, precious observation time has to be sacrificed.

However, due to a very harsh environment on board of the rocket, in terms of acceleration, shock, and vibration, as well as space constraints and extremely short observing time, a calibration system without any moving parts, a fully electronic calibration system, is the only option for PHOCUS. For example, a signal from a broadband calibrated noise source, instead of the hot load, could be injected through a directional coupler between the radio frequency horn (RF-horn) and the mixer as in Rose et al. (2009), but unfortunately at 183 GHz and 557 GHz such noise sources are not commercially available.

### 2.3 The 183 GHz RF channel calibration system

The driver for the 183 GHz calibration system on the PHOCUS rocket was to consider the above mentioned criteria, i.e. no moving parts and the space constraints. To achieve this, a calibration system with a stable pilot signal injected through a directional coupler (Meyer and Kruger, 1998) (−13 dB coupling) between the RF-horn antenna and the mixer was introduced. The pilot signal is placed 40 MHz away from the 183.31 GHz water absorption line, the target for the observation, and thus allows continuous calibration without any

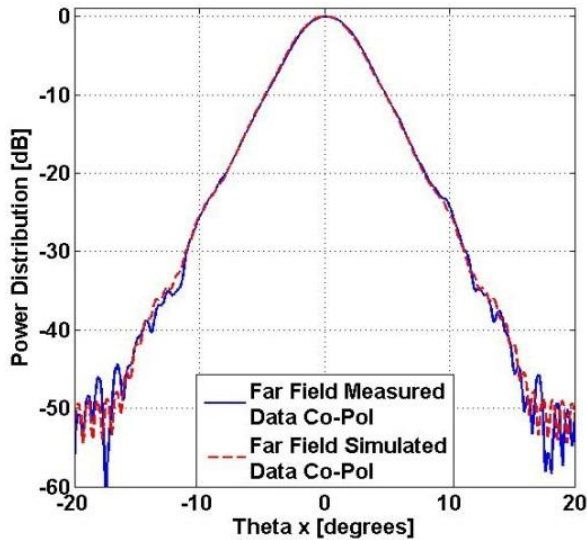


Fig. 6. Comparisons of Fourier transform of the near-field scan data at 183.31 GHz to PO-simulations.

loss of observation time. With this calibration technique, it is assumed that all receiver back-end channels experience the same gain variations over the observation time. The pilot signal is generated from the LO source for the 557 GHz radiometer, which has a base frequency of 15.727 GHz. The reference signal is extracted from the LO through a 20 dB directional coupler, amplified and fed into a harmonic mixer generating the pilot signal at 183.264 GHz (12th harmonic). The block diagram and layout of the radiometer with its calibration system can be seen in Fig. 3. The amplifier operates in saturation in order to keep the amplitude of the generated output calibration signal insensitive to small fluctuations in the reference signal supplied.

Right before the launch, the receiver noise temperature is measured by standard *Y*-factor technique in order to obtain an absolute temperature reference. This is done by placing hot (ambient temperature) and cold (LN2) loads outside the rocket, at the radiometer signal window. During this calibration, the level of the pilot signal referenced to the noise floor (ratio should be the same for hot- and cold loads) is recorded. During the flight, any drift of the gain in the receiver chain will result in a change in the pilot signal level relative to the baseline noise level.

#### 2.4 The 557 GHz IF channel calibration system

The 557 GHz radiometer calibration utilizes a different technique. This calibration system is also fully electronic, for the same reasons as pointed out in the previous section. The much higher frequency makes it more difficult and expensive to generate signals that could be used as a pilot signal, while, most importantly, introducing a directional coupler with its associated loss in front of the mixer would substantially

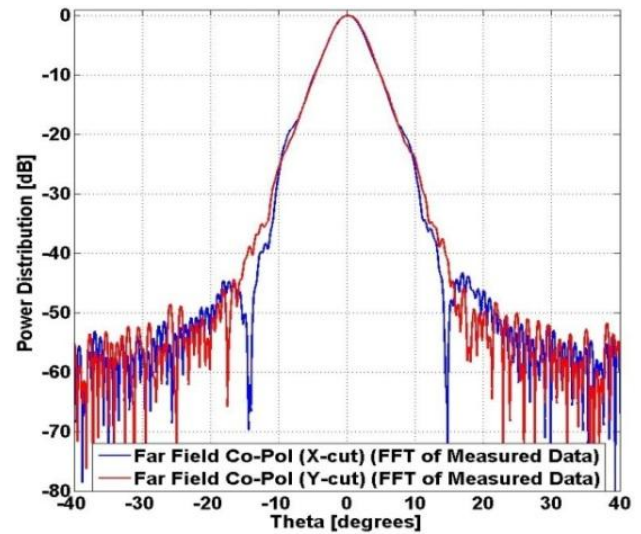


Fig. 7. Measured far-field pattern of the horn at 183.31 GHz.

increase the system noise. Following these considerations, the 557 GHz radiometer calibration is done by injecting broadband noise from a calibrated noise source, (Wireless Telecom Group, 2011), through a directional coupler between the mixer output and the first IF amplifier (LNA) (Fig. 4). This scheme limits calibration of the 557 GHz receiver channel to the gain to the IF and back-end parts, the parts probably mostly affected by changing the ambient temperature.

Since any measurements during the calibration would not be feasible, in contrast to the calibration system for the 183.31 GHz radiometer, the calibration is performed before the rocket reaches the altitude where the measurements should start. A second calibration is performed at the trajectory apogee, and the third calibration sequence is done once the rocket has reached an altitude below the altitude of interest. The drift in the receiver gain is measured between the baseline (independent on the load temperature) and the level with the calibration noise source switched on. A decrease in the receiver gain would result in a smaller difference between the on/off calibration signal cases.

#### 2.5 Horn design

The specifications of the far-field distribution for the 183 GHz and the 557 GHz radiometers required the beam width full width half maximum (FWHM)  $< 5^\circ$  with side-lobe level  $< -20$  dB. A typical optical design for such a narrow beam would be a combination of a horn and additional focusing elements, e.g. off-axis mirrors or a lens. However, as a consequence of a very limited space available inside the rocket, an optical layout with a single larger sized horn was chosen, since it provides the most compact alternative and

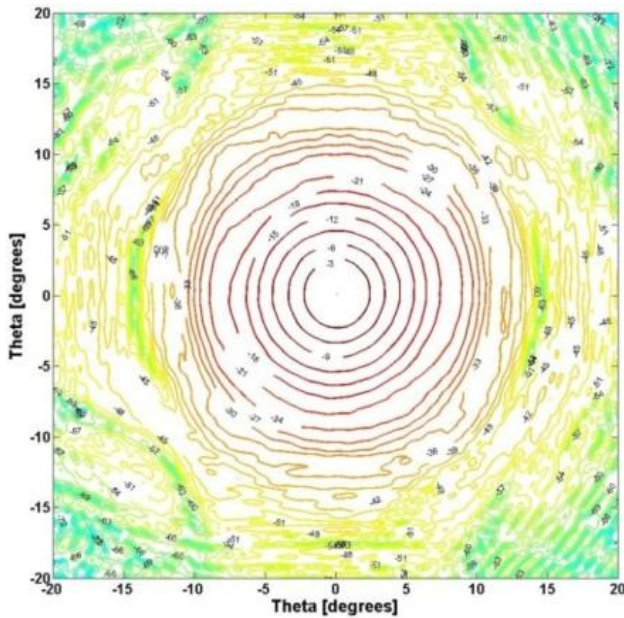


**Fig. 8.** Contour plot of the far-field pattern of the measured horn at 183.31 GHz.

reduces the complexity of placement and alignment of additional optical elements. A narrow beam requires large dimensions of the horn; consequently, the challenge is to obtain a large aperture while minimizing the length of the horn. Because of relatively narrow RF band required ( $183 \pm 0.02$  GHz and  $557 \pm 0.02$  GHz), we have chosen a smooth-wall conical horn. This type of horn is known to employ multi-mode field propagation inside the horn. In the literature, several horn types and horn profiles are presented in order to control the mode conversion and to reduce the length (Olver et al., 1994; Mahmoud, 1983; Watson et al., 1980; James, 1984; Potter, 1963; Pickett et al., 1984). The profiled horn shows very good performance for moderately compact sizes and FWHM of the order of  $10^\circ$  or wider. However, as a narrower beam is required, the side lobes tend to increase rapidly compared to a longer, linearly tapered, horn. Since the relative bandwidth of operation is less than 5%, a linearly tapered Pickett horn (Pickett et al., 1984), with a flared step, was selected for the design. In Kittara et al. (2007), the choice of a flared step is reported to be superior over the grooved step. The Pickett-Potter horn gives a moderately compact design with good performance over approximately 15% bandwidth and has the advantage over, for instance, the corrugated horn of simpler geometry and hence quicker production time. If necessary, bandwidth up to 30% can be achieved by adding more subsections in the horn, as reported in Yassin (2007). In the Potter horn, higher order modes are excited in the horn throat region by either a step discontinuity or a flared section (see Fig. 5). The idea behind the Potter horn is to excite, besides the dominant  $TE_{11}$  mode, the higher order  $TM_{11}$  mode.

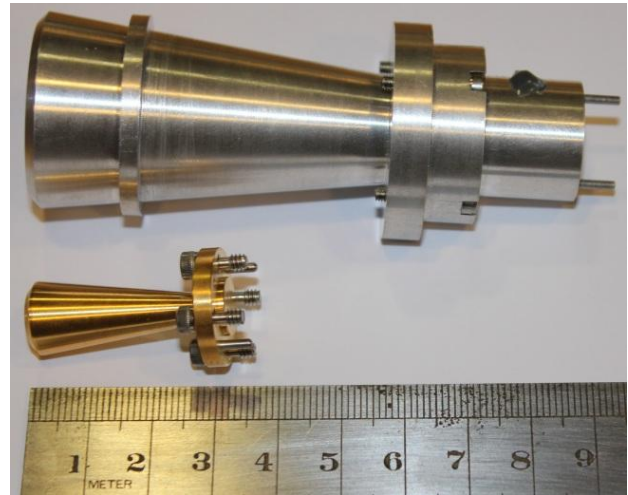


**Fig. 9.** Picture of the 183 GHz horn (top) and the 557 GHz horn (bottom).

In the conventional Potter horn design, the step discontinuity of the single-mode circular waveguide provides balanced transformation of approximately 16% of the dominant  $TE_{11}$  mode into the  $TM_{11}$  mode. This technique is referred to as the “dual-mode conical horn” and has the characteristic of side-lobe suppression and symmetric beam profiles (Potter, 1963). The original design, by P. D. Potter, has been further developed in order to create a more compact layout by removing the phasing section of the horn and use instead the length of the flared section to obtain the appropriate relative phase between the modes (Pickett et al., 1984).

In the horn design, presented here, the modal matching technique is used (Olver et al., 1994). This algorithm provides calculation of the modal conversion throughout the horn and the resulting modal content at the horn aperture. As pointed out in Kittara et al. (2007), other higher order modes apart from the  $TM_{11}$  mode will exist in the horn, and excitation of, for example, the  $TE_{12}$  mode at specific relative amplitude and phase at the horn aperture could help improve the bandwidth performance. In the present horn design, we try to employ, besides the  $TE_{11}$ ,  $TM_{11}$ , and  $TE_{12}$  modes, other higher order modes. For this purpose a mode matching software was used in conjunction with a Matlab (Matlab, 2011) optimization routine, which finds the optimum mode content at the aperture for the desired far-field distribution. The optimization function uses a modified version of the built-in optimization routine with bound constraints on the variables, *fminsearchbnd* (D’Errico, 2005). The function is based on the Nelder-Mead simplex search method (Lagarias et al., 1997). In the design, the goals are specified as (i) desired beam width, (ii) low side-lobe levels and circularity, and (iii) return loss below  $-30$  dB. The optimization variables are shown in Fig. 5, where  $h_1$  and  $\alpha$  define the step, and  $\beta$  and  $L$  the horn conical section to obtain the desired

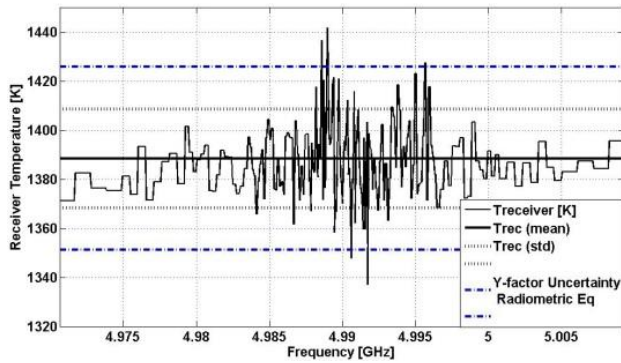


**Fig. 10.** Laboratory measurements of the 183 GHz receiver noise temperature.

modal phases at the horn aperture. The mode matching software used assumes that the discontinuity is excited only by modes of the  $TE_{1n}$  and  $TM_{1n}$  type, and, due to symmetry of the junction, only modes of the  $TE_{1n}$  and  $TM_{1n}$  may be excited. In Table 2, the amplitude and phase of the first five  $TE_{1n}$  and  $TM_{1n}$  are shown.

The final design was verified with physical optics (PO) software, MODAL, developed by NUIM (Gradziel, 2011), which showed excellent agreement to the measured data (Fig. 6).

The 183 GHz horn for SondRad was made out of aluminium alloy by machining with a computer-controlled lathe. It was measured using Agilent PNA 8364B (Agilent Technologies Inc., 2011) with frequency extension modules (OML Inc., 2011). The far-field pattern of the horn was calculated via a Fourier transform of the near-filed scan and is shown in Figs. 7 and 8 with a FWHM of  $4.7^\circ$  and side-lobe levels less than  $-40$  dB.

The 557 GHz horn is an exact scaled version of the 183 GHz horn, but no measurements were performed because of the absence of suitable equipment at this frequency. The 557 GHz horn was produced by Radiometric Physics GmbH (Radiometric Physics GmbH, 2011) by electroforming, and the horn performance is expected to be the same as for the 183 GHz horn relying on exact scaling effect. Pictures of the two horns are presented in Fig. 9.

### 3 Laboratory measurements

#### 3.1 Laboratory measurements of the 183 GHz calibration system

The receiver temperature and the pilot signal measurements performed in the laboratory are presented in Figs. 10 and 11. The mean value and standard deviation are plotted together with the noise temperature, where the mean is calculated for the central channels where the resolution is the highest, 67 kHz. At the band edges, the channels are combined in order to reduce the data storage. The data in Figs. 10

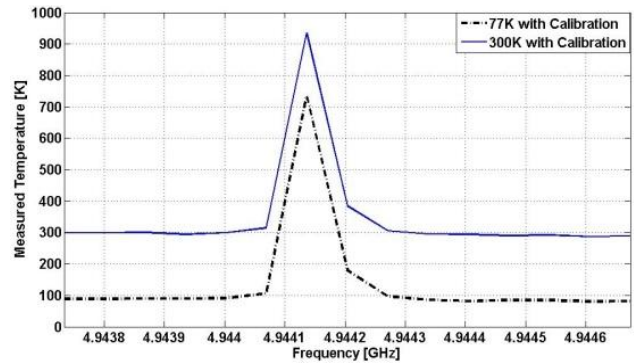


**Fig. 11.** Pilot signal with liquid nitrogen and room temperature loads.

and 11 are integrated over 10 s, and the calibration accuracy (repeatability) is estimated to be less than 2 % and is calculated as

$$\Delta = (\text{Peak Hot} - \text{Baseline Hot}) - (\text{Peak Cold} - \text{Baseline Cold}) \quad (4)$$

$$\text{Uncertainty}(\%) = \frac{\Delta}{\text{Peak} - \text{Baseline}} \times 100 \quad (5)$$

During the observation period, the measurement rate is 300 Hz, resulting in an integration time of 3.3 ms per spectrum. In order to determine if the required integration time for the observation is allowed by the actual stability of the receiver, its output was measured and the Allan variance was calculated. Notice that the integration time in order to obtain a stable pilot signal is independent of the integration time used for the observation data, which might be shorter in order to dissect the mesosphere and obtain the desired altitude profile. The observations will typically be in blocks of 0.1 s, i.e. integration over 30 spectra. The Allan variance of the 183 GHz radiometer is shown in Fig. 12 for both the observation channels and the channel where the pilot signal is located. Longer measurements are needed in order to find the integration limit, but the internal memory in the backend has limited capacity, and the measurements over time periods  $>150$  s are not possible due to the limited data storage capacity. During the flight, measurement time will be less than 100 s, and after the data are stored on an SD-card and USB-memory and the internal memory is cleared, a new measurement session can take place.

#### 3.2 Laboratory measurements of the 557 GHz calibration system

The stability for the 557 GHz receiver was measured by sampling the output signal, and the Allan variance time was calculated in order to obtain the optimum integration time. Figure 13 shows the Allan variance plots for the receiver without and with the calibration noise source switched on.

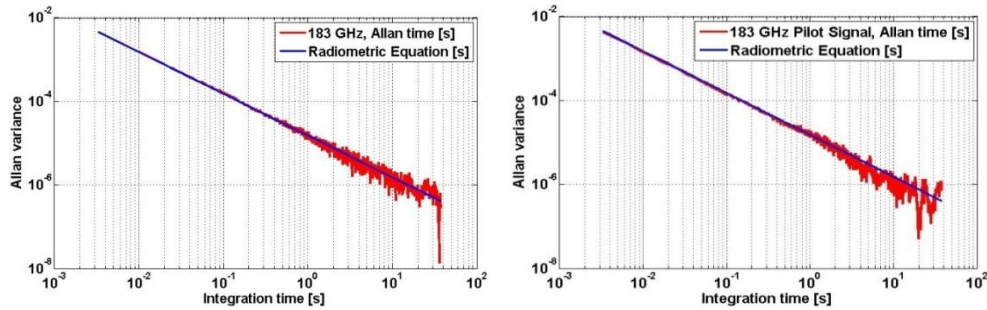


Fig. 12. Allan variance for the 183 GHz receiver (left) and the Allan variance for the receiver channel containing the pilot signal.

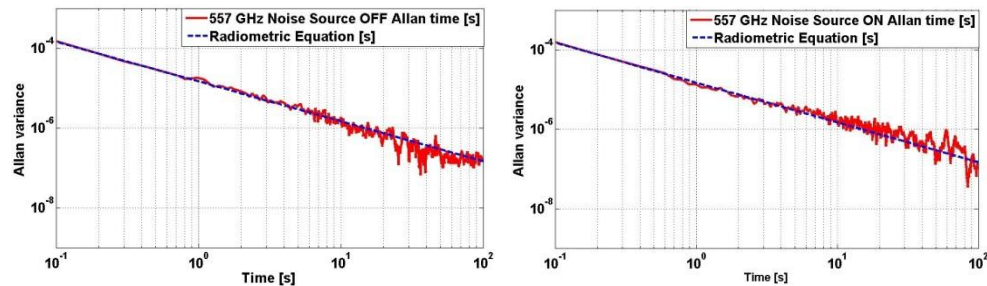


Fig. 13. Allan variance plots (77 K load) with the noise source off (left) and the noise source on (right).

It can be seen in Fig. 13 that the Allan variance plot agrees very well with the radiometric equation, Eq. (1), i.e. the white noise component prevails over  $1/f$  noise for the represented time scale. The total flight period (one way) of approximately 60–100 s (nose cone ejection – apogee) is well within the measured Allan variance. During flight, calibration with an integration time of approximately 5 s was used for this radiometer, which is well within the feasible integration time with the source on.

The receiver temperature is also dependent on the physical temperature surrounding the instrument; hence the receiver temperature might differ from the laboratory measurements, where a fan was used for cooling. Figure 14 shows two different laboratory measurements, with and without fan cooling (fan directed towards the back end). It can be seen that the receiver noise temperature has increased by 179.9 K (mean value) when the receiver physical temperature is increased by  $2.4^{\circ}\text{C}$  for the 557 GHz front end and  $15.7^{\circ}\text{C}$  for the back end. The mean value, standard deviation, and uncertainty of the  $Y$ -factor measurement are plotted. The uncertainty in the  $Y$ -factor measurement is estimated by the use of the radiometer equation. With a system temperature of 4200 K, a bandwidth of 67 kHz, and the integration time of 10 seconds, this gives a standard deviation of 5.13 K. This accuracy leads to an uncertainty in the cold measurement of 6.41 % and 1.71 % at 300 K. A total uncertainty in the  $Y$ -factor of 8.1 % results in an uncertainty of 340.5 K in the receiver noise temperature.

Figure 15 shows the measured temperature for 80 K and 300 K, and with the noise signal switched on. This figure illustrates well the concept of the calibration method, where the difference in level between the baseline with and without the noise source should be the same independent on the antenna temperature. If the system gain varies, this difference will vary as well, i.e. a drop in the system gain would result in a decrease in the difference of the levels (source on/off).

In Fig. 16, the calibration error, i.e. the uncertainty of the temperature levels relative to the baseline, is plotted for the two measurements with different physical, stable, physical operating temperatures. This is the difference between the calibration level and the baseline level, as the load temperature is changed from 80 K to 300 K calculated as

$$\text{err} = ((300 \text{ K} + \text{Noise ON}) - (300 \text{ Kload})) - ((80 \text{ Kload} + \text{Noise ON}) - (80 \text{ Kload})), \quad (6)$$

and it can be seen that the standard deviations of the calibration, over the central channels, are approximately the same in the two measurements: 11.3 K and 13.7 K (7 K over all channels).

The standard deviation of 12 K can be compared to the fluctuations between channels in two consecutive measurements performed with an 80 K load (Fig. 17). The level of fluctuations between channels is less in this case, with a standard deviation 7.9 K (4.2 K over all channels) compared to 12 K (7 K) with the noise source. The higher fluctuation in the calibration is expected, since the system noise temperature ( $T_{\text{receiver}} + T_{\text{antenna}}$ ) is significantly higher (1300 K)

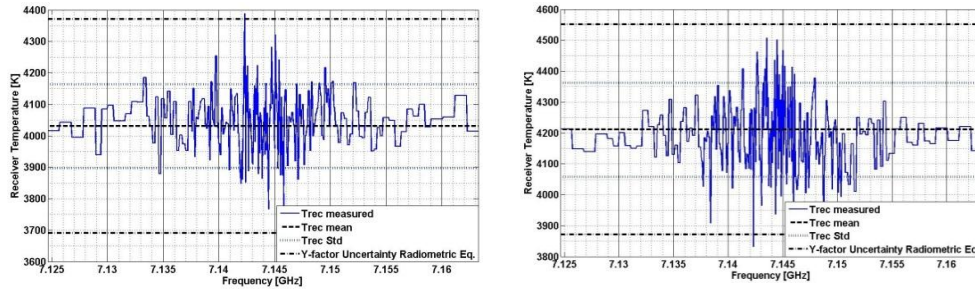


Fig. 14. Laboratory measurements of the receiver temperature with fan cooling (left) and without cooling (right).

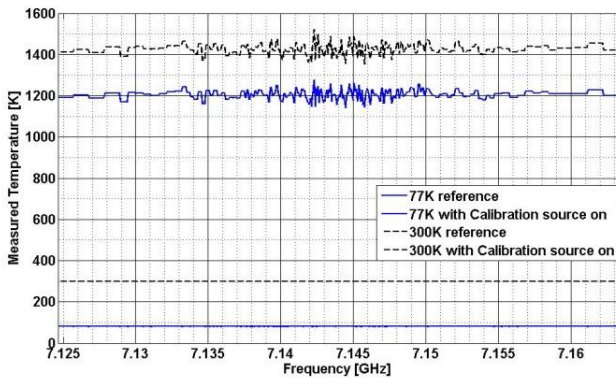


Fig. 15. Measured temperature (in the load coordinate system) for 80 K and 300 K and with the noise signal switched on.

with the noise source switched on. The standard deviation is slightly higher than calculated theoretical values based on the radiometric equation, resulting in a standard deviation of 5 K for the measurements of the 80 K load ( $T_{\text{system}} = 4100$  K) and 6.6 K for the measurements with the noise source switched on ( $T_{\text{system}} = 5400$  K). Prior to the rocket lift-off, a liquid cooling system is engaged and attached to the backend base plate in order to avoid the temperature rising, if the count-down is put on hold for a long time.

Absolute receiver noise temperature measurement prior to flight will not be possible due to the rocket nose cone placement, but the calibration procedure for gain variations is independent on the physical temperature of the instrument and the antenna load; hence, a reference for the gain variations is obtained by switching on/off the calibrated noise source. In Fig. 18, the calculated receiver noise temperature for the two measurements with different physical temperatures of the receiver is plotted. Included in the plot is also the corrected curve of measurement no. 2, i.e. the measurement at a higher physical temperature calibrated with respect to measurement no. 1. The calibration procedure is performed by calculation of the ratios of the radiometer counts between the antenna signal and with the calibrated noise source switched on for both measurements:

$$\Delta_1 = \frac{\text{Calibration 1 (Counts (Load))}}{\text{Calibration 1 (Counts (Load + Noise Source))}} \quad (7)$$

$$\Delta_2 = \frac{\text{Calibration 2 (Counts (Load))}}{\text{Calibration 2 (Counts (Load + Noise Source))}} \quad (8)$$

The Y-factor is then corrected by the difference in the ratios as

$$Y_{\text{factor corrected}} = Y_{\text{factor}} + (\Delta_1 - \Delta_2). \quad (9)$$

The residual difference after calibrating the spectra is  $< 50$  K, which results in a calibration uncertainty  $< 1.25\%$ , assuming 4000 K receiver noise temperature.

#### 4 Discussion on flight results and post-flight calibration

The laboratory results presented in the previous sections were performed at temperatures in the range 25–35 °C. At each measurement session, the physical temperature of the instrument was stable ( $< \pm 0.05$  °C). The calibration system was designed based on the assumption that the instrument temperature would be reasonably stable during the short observation period, for which laboratory measurements of the calibration system have indicated reliable performance. Figures 19 and 20 show laboratory measurements of the radiometric counts and temperature over 100 s together with a linear fit of the data. The temperature and the pilot signal amplitude remain constant with self-heating of the instrument and an engaged table fan for temperature stabilization.

However, we observed that the instrument temperature increased significantly after the launch, with the temperature changing from 16 to 28 °C over the observation period. That makes the assumption of stable physical temperature obviously not valid. The extreme increase in the temperature, 12 °C over less than 4 min (!), was not expected, since the same increase in temperature during laboratory measurements takes almost 1.5 h. The exact cause of the temperature rise is not clear, but the major difference between laboratory measurements and the flight sequence is the lack of cooling through convection at high altitudes. A rise in temperature of the rocket structure was expected but should not exceed 70–80 °C, and there are only a few attachment points between

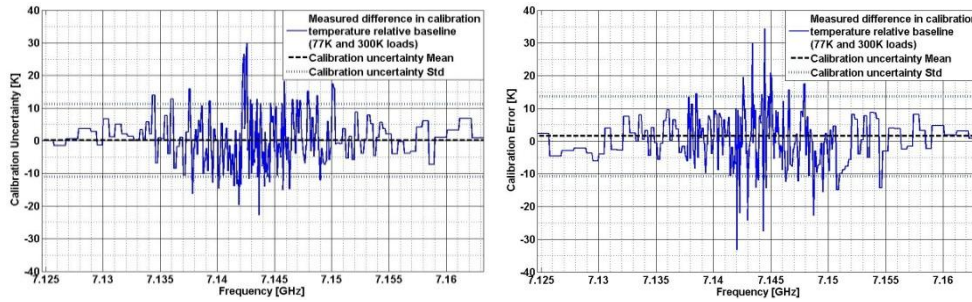


**Fig. 16.** Calibration uncertainty of the receiver calibration for two different physical temperature of the receiver. The calibration uncertainty remains unaffected for a increase in receiver noise temperature of 136 K. The central channels with 67 kHz bandwidth is considered in the calculations.

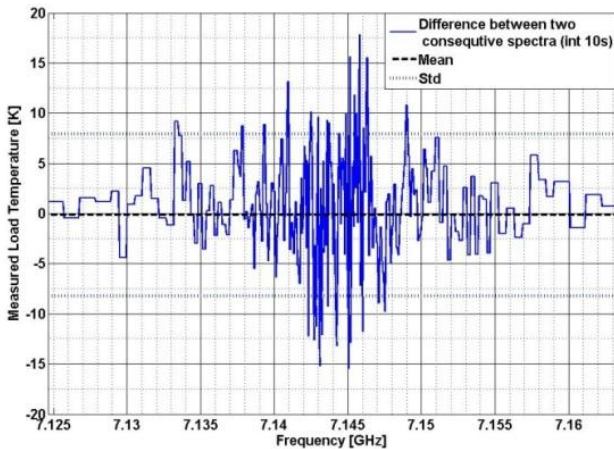


**Fig. 17.** Two consecutive 10 s measurements performed with a load temperature of 77 K: the standard deviation over the central channels is 7.9 K, compared to 12 K with the noise source switched on.

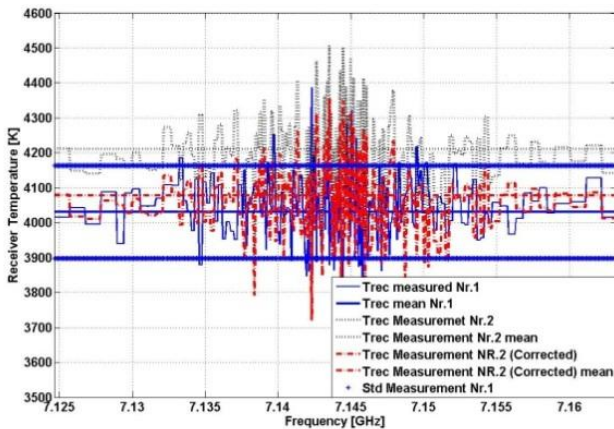


**Fig. 18.** Measured receiver noise temperature for two measurements with different physical temperatures of the receiver and the calibrated curve. The calibrated curve shows a residual offset of 46.23 K, which indicates a calibration error of 1.16 %.

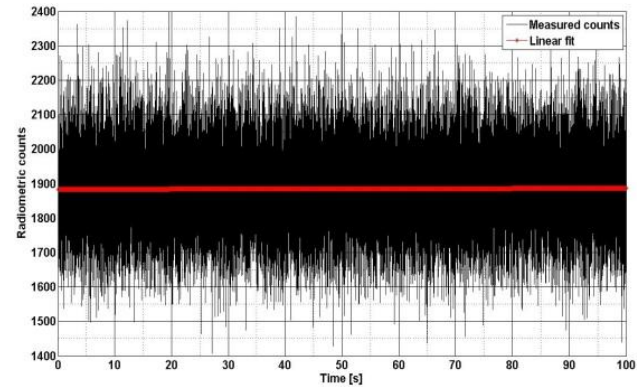


**Fig. 19.** Laboratory measurements of radiometric counts over time with a stable physical temperature. The temperature is shown in Fig. 20.

the outer structure and the 183 GHz radiometer base plate that could transfer heat. Further, heating through radiation from the outer structure to the base plate would not cause this significant rise over the short flight period. The only significant heat source present is the backend (producing 70 W of heat) that shares the same heat sink as the 183 GHz front-end instrument and the points where the front end plates are attached to the rocket structure.

In order to investigate the temperature dependence of the 183 GHz front-end base plate due to the different heat sources in assumption of being placed in vacuum environment, the FEM simulation software ANSYS (ANSYS Inc., 2011) was used. The simulation models are shown in Fig. 21 with the temperatures indicated on the position of the front-end receiver (Point A) and further out on the base plate (Point B). The initial temperature of the base plate was set to 16 °C, corresponding to the initial value during flight, and the end temperature was simulated after 240 s, the time after which the instruments are switched off in the flight sequence. The simulated temperatures caused by different heat sources at probe positions A and B are shown in Table 1.

**Table 1.** Temperature variation due to different heat sources simulated with FEM software ANSYS. Initial temperature of the front-end base plate was set to 16 °C. Points A and B are referred to Fig. 21.

Time [s]	Heat source					
	Backend (70 W)		Radiation (80 °C)		Backend + Radiation + Heat flow through interface points	
	Probe A	Probe B	Probe A	Probe B	Probe A	Probe B
Temp. probes						
0	16 °	16 °	16 °	16 °	16 °	16 °
240 (end of flight sequence)	17.8 °	18.5 °	16.4 °	16.5 °	23.4 °	27.8 °

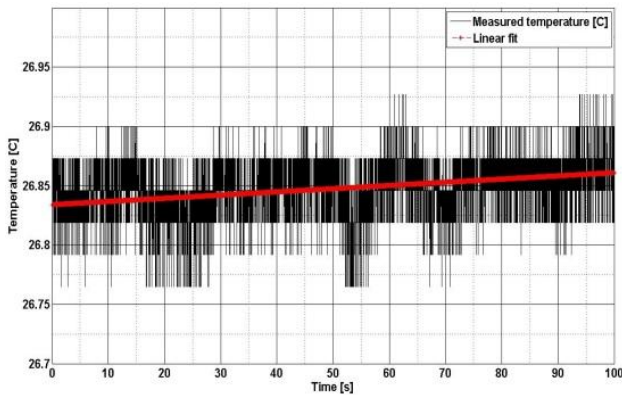


**Fig. 20.** Laboratory measurements of temperature variation over time with self-heating of the instrument and a table fan.

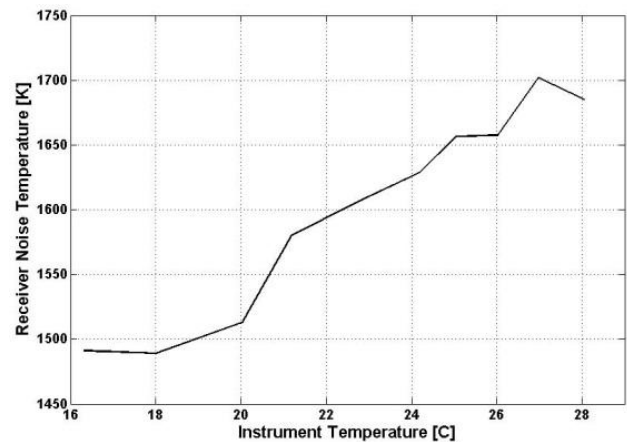


**Fig. 22.** Laboratory measurements of receiver noise temperature vs. increase in physical temperature of the instrument.

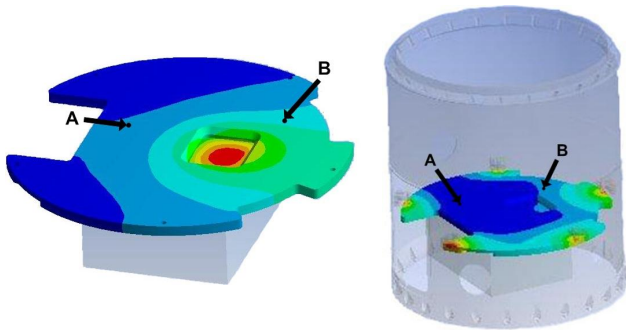


**Fig. 21.** ANSYS-simulations of temperature variations with different heat sources. To the left, only heat (70 W) due to the backend is included. To the right, two different simulations are performed: temperature increase due to radiation from the rocket structure alone and increase due to radiation, heating through thermal conduction from the backend, and heat conduction through the mounting points between the outer structure and the front-end base plate. The temperature increase is shown in Table 1.

It can be concluded from the simulations that the major contribution to the temperature increase is due to the thermal flow from the outer structure of the rocket through the

mounting points on the 183 GHz front-end base plate. Still, the simulations show 5 °C lower temperature for position A (the location of the front-end) at the end of the flight sequence than during the actual flight, indicating presence of additional heat sources. A real uncertainty is the actual temperature of the outer structure of the rocket, since this is only an estimation based on information provided by T. Karlsson and K. Sjölander (personal communication, 2011), and its impact on the final temperature is significant.

As it turned out, this increase in temperature had severe impact on the 183 GHz calibration system, and a significant drop in the pilot signal amplitude was observed. This drop was clearly too large to be the effect of system gain variation, which was derived from calibration measurements at different temperatures made both before and after launch. Fortunately, the instruments were perfectly intact after landing and recovery of the rocket payload, and post-flight measurements of the instrument behaviour with different operating temperatures could be performed in order to pin-point the most sensitive components and to draw conclusion of what should be changed in order to improve the design.

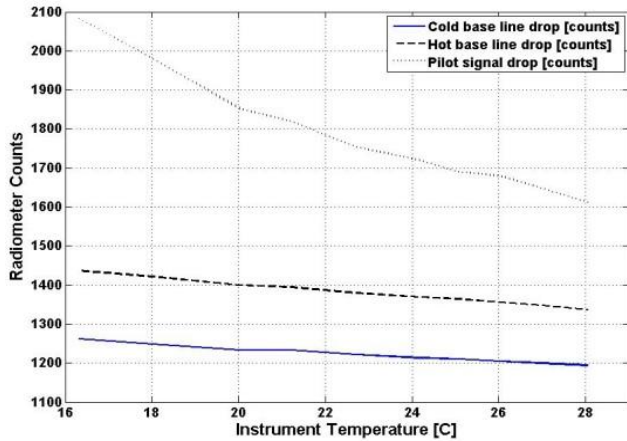


Fig. 23. Laboratory measurements of radiometer counts vs. increase in physical temperature of the instrument.

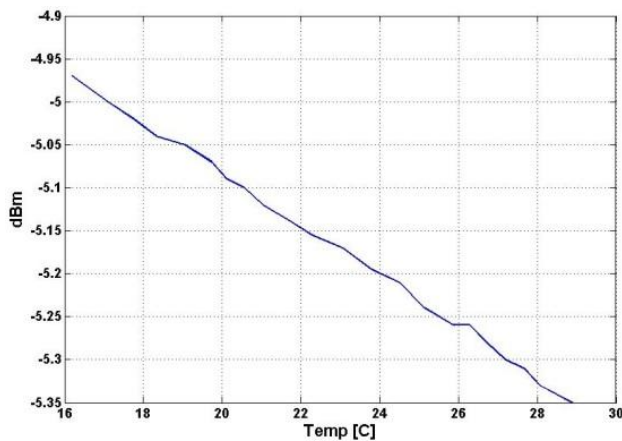


Fig. 24. Output power of the reference oscillator vs. physical temperature of the instrument.

For the post-flight measurements, the instrument is cooled down to the initial temperature of the flight using a climate chamber, and  $Y$ -factor measurements as well as measurements of signal levels at different points in the system are performed as the temperature of the instrument increases. The  $Y$ -factor measurements show an increase of the receiver noise temperature with increasing physical temperature of the instrument and are presented in Fig. 22. In addition, the radiometric counts vs. temperature decrease with an increase in temperature with a constant load temperature at the RF-input, indicating a drop in gain in the system. In Fig. 23, where the radiometric counts vs. temperature are plotted for liquid nitrogen and room temperature loads, it is also clear that the pilot signal behaviour has significant temperature dependence.

In order to investigate the critical components, the following measurements were performed as a function of the ambient temperature: (1) signal output level from the oscillator

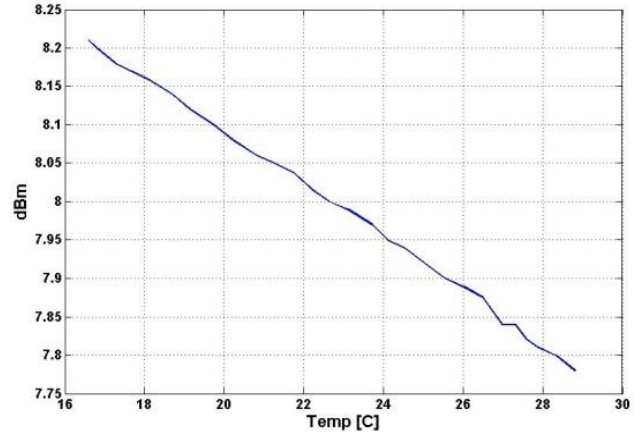


Fig. 25. Output power of the amplifier in the calibration path vs. physical temperature of the instrument.

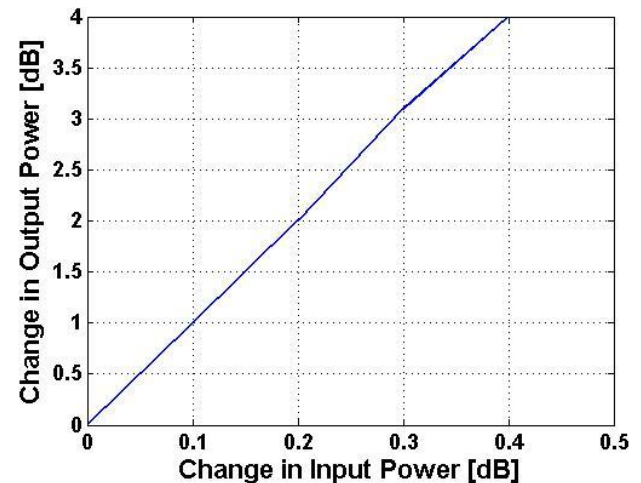


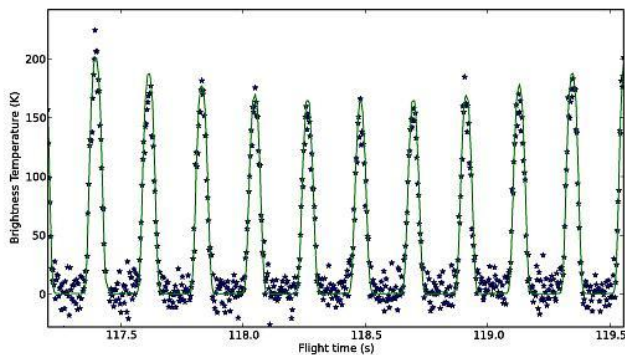
Fig. 26. Response of the output power at the 12th harmonic of the harmonic mixer as a function of input power.

providing reference signal for the calibration signal (and the 557 GHz LO); (2) signal output level after the amplifier in the calibration path. The results from (1) and (2) are presented in Figs. 24 and 25.

It can be seen that the signal level drops 0.36 dB for (1) and 0.42 dB for (2) over the temperature range 16–28 °C. The similar drop of the amplifier output indicates that the amplifier might not have been saturated sufficiently. On the other hand, a saturated amplifier could be more sensitive to a temperature increase. The next step was to investigate the power level of the 12th harmonic from the harmonic mixer producing the pilot signal close to water line at 183 GHz, since the power drop observed in the radiometer counts was larger than 0.42 dB. To measure the spectral power at these frequencies is very challenging, since the output power level is very low (pW) and a broadband power-meter would not be sufficient. In order to determine the change in output power level as

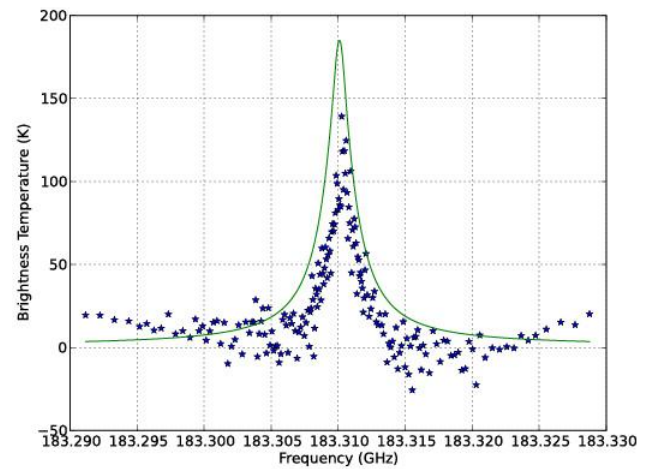
**Table 2.** First five TE<sub>1n</sub> and TM<sub>1n</sub> modes present at the horn aperture.

Modes	Magnitude	Phase [deg]
TE <sub>11</sub>	0.766	37.0
TM <sub>11</sub>	0.473	78.0
TE <sub>12</sub>	0.352	110.4
TM <sub>12</sub>	0.194	-163.5
TE <sub>13</sub>	0.121	-121.0
TM <sub>13</sub>	0.083	-36.8
TE <sub>14</sub>	0.055	29.0
TM <sub>14</sub>	0.023	106.9
TE <sub>15</sub>	0.026	-173.3
TM <sub>15</sub>	0.006	-36.5

**Fig. 27.** Average brightness temperature at 183.195 GHz  $\pm$  3.5 MHz showing roll modulation as the FOV sweeps between  $-10$  and  $10$  degs elevation. Asterisks (\*) show the measured signal, and the solid line is a simulation using an approximate atmospheric model.

the input power to the harmonic mixer changes, the ALMA Band 5 (Billade, 2009) SIS-receiver was used. This provides the possibility to measure the relative spectral power as the input level changes. The measurements show a change of  $(\Delta 1 \text{ dB output power})/(\Delta 0.1 \text{ dB input power})$ , shown in Fig. 26.

From the post-flight measurements, it is clear that a very accurate temperature stabilization system is needed for the calibration circuit, if a pilot signal generated by a harmonic mixer is to be used as a reference signal for calibration. Laboratory measurements show that the temperature stability of the calibration signal path should be  $< \pm 0.05 \text{ }^\circ\text{C}$  for a stable reference signal. Clearly, the front-end base plate needs to be thermally isolated from the outer structure of the rocket as well as from the backend in order to minimize heating of the instruments. The system could also be improved significantly by introducing a separate, temperature-stabilized, oscillator for the pilot signal and a temperature stabilization system for the amplifier. Additional radiation shields, between the back-end heat-sink and the front-end base plate and between the rocket structure and the instruments, should keep heat transfer through radiation to a minimum, even if simulations show

**Fig. 28.** The measured spectrum (\*) at 0–3 deg elevation and a rocket altitude of 57 km compared with a simulation using an approximate atmospheric model. Note that the calibration applied to the measurements is only approximate and based on the temperature dependent calibrations carried out before launch.

that this contribution is minor. With these improvements in the design, a very stable operating temperature of the calibration system should be possible. The total power dissipation of a separate oscillator and amplifier should be no more than 4 W of power, making a thermoelectric cooler a good candidate to achieve a very stable operating temperature.

## 5 Flight calibration using rocket pointing and atmosphere temperatures

For the 183 GHz channel, it may be possible to use the actual measurements to calibrate the radiometer gain. As illustrated in Fig. 27, the measured signal is expected to vary around a rotation from fully saturated to near zero, as the field of view of the instrument is swept through elevations of typically  $-10$  to  $+10$  degrees. The figure is for the signal integrated over the first 10 channels, and thus it can be expected that most channels will exhibit such behaviour over most of the flight. Simulations have been performed using the AM-ATERASU package (Baron et al., 2008) using realistic atmospheric temperatures and pressures based on the ECMWF analysis for the day of the rocket flight and two very different water vapour profiles. The result indicates that, if the temperature profile is reasonable, differences in water vapour will not affect the calibration as long as the central channels are avoided. This approach has however to be compared to the pre- and post-flight calibrations and fully verified through further analysis. In Fig. 28 a measured spectrum at 0–3 deg elevation and a rocket altitude of 57 km compared to a simulation using an approximate atmospheric model is shown.

## 6 Conclusions

A radiometer comprising two frequency channels (183 GHz and 557 GHz) for observing the respective water lines has been constructed and flown on board of Swedish PHOCUS rocket. The radiometers include novel calibration systems specifically adjusted for use with each frequency channel. The first results indicate that the instrument successfully performed measurements of the mesospheric water profile as planned. An example spectrum is shown in Fig. 28 compared to a simulation based on a model atmosphere. However, the temperature environment for the instruments has shown more extreme behaviour than expected and accounted for. Consequently, the results of the calibration and the final data reduction will need careful treatment. Useful lessons such as thorough thermal simulations of the structure are needed to provide reliable thermal designs. More extensive data on the heating effects on the rocket outer shell are needed to improve accuracy of the thermal modelling. Additionally, modifications in the mechanical design are needed to provide thermal decoupling of the receiver heat-sink from the rocket structure as well as from the backend system. Further, a separate, temperature-stabilized, calibration system should be implemented when a pilot signal is used as calibration source.

*Acknowledgements.* The authors would like to acknowledge Thomas Karlsson and Krister Sjölander at SSC for useful discussion on the instrument-rocket interface design, Sven-Erik Ferm (GARD) for producing the 183 GHz horn and Magnus Strandberg (GARD) for assisting with thermal simulations. The authors would also like to thank the people at Omnisys Instruments AB, Terese Ekebrand, Christina Emrich, Mikael Krus, and Anders Emrich for our cooperation and their assistance in the instrument testing. Further the authors thank Philippe Baron for his help in using AMATERASU for the simulations. Funding for this experiment was provided by the Swedish Research Council VR and the Swedish National Space Board.

Edited by: J. Gumbel

## References

- Agilent Technologies Inc.: available at: [www.home.agilent.com](http://www.home.agilent.com), last access: 5 December 2011.
- Allan, D. W.: Statistics of atomic frequency standards, *Proc. IEEE*, 54, 221–230, 1966.
- ANSYS Inc.: ANSYS simulation software, available at: [www.ansys.com](http://www.ansys.com), last access: 5 December 2011.
- Baron, P., Mendrok, J., Kasai, Y., Ochiai, S., Seta, T., Sagi, K., Suzuki, K., Sagawa, H., and Urban, J.: AMATERASU: Model for atmospheric TeraHertz Radiation analysis and simulation, *Journal of the National Institute of Information and Communications Technology*, 55, 109–121, 2008.
- Becker, E. and Fritts, D. C.: Enhanced gravity-wave activity and interhemispheric coupling during the MaCWAVE/MIDAS northern summer program 2002, *Ann. Geophys.*, 24, 1175–1188, doi:10.5194/angeo-24-1175-2006, 2006.
- Billade, B.: Design Of Dual Polarisation Sideband Separation Mixer For ALMA Band 5, Tech. Lic.-thesis Chalmers University of Technology, Tech. Lic., 2009.
- Croskey, C. L., Olivero, J. J., Puliafito, S. E., and Mitchell, J. D.: ROCKETMAS: A sounding-rocket-based remote sensing measurement of mesospheric water vapour and ozone, *ESA SP-355*, 213–217, 1993.
- D'Errico, J.: The Mathworks Inc., available at: [www.mathworks.com/matlabcentral/fileexchange/8277-fminsearchbnd](http://www.mathworks.com/matlabcentral/fileexchange/8277-fminsearchbnd) (last access: 5 December 2011), 2005.
- Dicke, R. H.: The Measurement of Thermal Radiation at Microwave Frequencies, *Rev. Sci. Instrum.*, 17, 268–275, doi:10.1063/1.1770483, 1946.
- Ekebrand, T.: SondRad Operation Manual, internal document, 2011.
- Gradziel, M.: MODAL, Department of Experimental Physics, National University of Ireland, Maynooth, Ireland, 2011.
- Gumbel, J.: Atmospheric science with sounding rockets – present status and future perspectives, 18th ESA Symposium on European Rocket and Balloon Programmes and Related Research ESA, 2007.
- Hervig, M. and Siskind, D. E.: Decadal and inter-hemispheric variability in polar mesospheric clouds, water vapor, and temperature, *J. Atmos. Sol.-Terr. Phys.*, 68, 30–41, doi:10.1016/j.jastp.2005.08.010, 2005.
- James, G.: Design of wide-band compact corrugated horns, *Antennas and Propagation, IEEE T. Antenn. Propag.*, 32, 1134–1138, 1984.
- Khaplanov, M., Gumbel, J., Wilhelm, N., and Witt, G.: Hygrosonde – A direct measurement of water vapour in the stratosphere and mesosphere, *Geophys. Res. Lett.*, 23, 1645, doi:10.1029/96GL01482, 1996.
- Kittara, P., Jiralucksanawong, A., Yassin, G., Wangsuya, S., and Leech, J.: The Design of Potter Horns for THz Applications Using a Genetic Algorithm, *Int. J. Infrared Milli.*, 28, 1103–1114, 2007.
- Lagarias, J. C., Reeds, J. A., Wright, M. H., and Wright, P. E.: Convergence Properties of the Nelder-Mead Simplex Method in Low Dimensions, *SIAM J. Optimiz.*, 9, 112–147, 1997.
- Mahmoud, S. F.: Mode conversion on profiled corrugated conical horns. *Microwaves, Optics and Antennas, IEE Proceedings on Microwaves, Optics and Antennas*, 130, 415–419, 1983.
- Matlab: The Mathworks Inc., available at: [www.mathworks.com/products/matlab/](http://www.mathworks.com/products/matlab/) (last access: 5 December 2011), 2011.
- Meyer, P. and Kruger, J. C.: Wideband crossed-guide waveguide directional couplers, *Microwave Symposium Digest, 1998 IEEE MTT-S International*, 1998.
- National Aeronautics and Space Administration, NASA: available at: [www.nasa.org/mission\\_pages/aim](http://www.nasa.org/mission_pages/aim), last access: 1 May 2012.
- Olver, A. D., Clarricoats, P. J. B., Kishk, A. A., and Shafai, L.: ISBN: 0 7803 1115 9, published by: The Institution of Electrical Engineers, London, UK, and the Institute of Electrical and Electronics Engineers, Inc., New York, USA, 1994.
- OML Inc.: available at: [www.omlinc.com](http://www.omlinc.com), last access: 5 December 2011.
- Omnisys Instruments AB: available at: [www.omnisys.se](http://www.omnisys.se), last access: 5 December 2011.

- Pickett, H. M., Hardy, J. C., and Farhoomand, J.: Characterization of a Dual-Mode Horn for Submillimeter Wavelengths (Short Papers), *Microwave Theory and Techniques*, IEEE Transactions on Microwave Theory and Techniques, 32, 936–937, 1984.
- Potter, P. D.: A New Horn Antenna with Suppressed Sidelobes and Equal Beamwidths. Jet Propulsion Laboratory, California Institute of Technology, Pasadena, CA, USA, Technical 30 Report No. 32-354, 1963.
- Radiometric Physics GmbH: available at: <http://www.radiometer-physics.de>, last access: 5 December 2011.
- Rapp, M. and Lübken, F.-J.: Polar mesosphere summer echoes (PMSE): Review of observations and current understanding, *Atmos. Chem. Phys.*, 4, 2601–2633, doi:10.5194/acp-4-2601-2004, 2004.
- Rapp, M. and Thomas, G. E.: Modelling the microphysics of mesospheric ice particles: assessment of current capabilities and basic sensitivities, *J. Atmos. Sol.-Terr. Phys.*, 68, 715–744, 2006.
- Rohlfs, K. and Wilson, T.: *Tools of Radio Astronomy*, 3rd Edn., 2000.
- Rose, T., Czekala, H., and Mombauer, A.: Microwave Radiometer Systems for Profiling of Low Water Vapour Concentrations and Temperature, in: *Antarctica and for Polarized Observations of Rain: Instruments, Retrievals and Results*, 8th Int. Symp. on Tropospheric Profiling, Delft, The Netherlands, 2009.
- Stevens, M. H., Gumbel, J., Englert, C. R., Grossmann, K. U., Rapp, M., and Hartogh, P.: Polar mesospheric clouds formed from space shuttle exhaust, *Geophys. Res. Lett.*, 30, 1546, doi:10.1029/2003GL017249, 2003.
- Stevens, M. H., Englert, C. R., DeLand, M., and Hervig, M.: The polar mesospheric cloud ice mass in the Arctic summer, *J. Geophys. Res.*, 110, A02306, doi:10.1029/2004JA010566, 2005.
- Thomas, G. E.: Mesospheric clouds and the physics of the mesopause region, *Rev. Geophys.*, 29, 553–575, 1991.
- Thomas, G. E., Olivero, J. J., Jensen, J. E., Schroeder, W., and Toon, O. W.: Relation between increasing methane and the presence of ice clouds at the mesopause, *Nature*, 338, 490–492, doi:10.1038/338490a0, 1989.
- Thomas, G. E., Olivero, J. J., DeLand, M., and Shettle, E. P.: A response to the article by U. von Zahn. Are noctilucent clouds truly a miner's canary of global change?, *EOS T. Am. Geophys. Un.*, 84, 352–353, 2003.
- Virginia Diodes Inc.: available at: [www.vadiodes.com](http://www.vadiodes.com), last access: 5 December 2011.
- Watson, B., Rudge, A., Dang, R., and Olver, A.: Compact low-cross polar corrugated feed for E.C.S, *Antennas and Propagation Society International Symposium*, 1980.
- Wireless Telecom Group, I.: available at: [www.noisecom.com](http://www.noisecom.com), last access: 5 December 2011.
- Yassin, G.: A High Performance Horn for Large Format Focal Plane Arrays, *Proc. of 18th Int. Sym. on Space Terahertz Technology*, Pasadena, CA, USA, 2007.
- Zahn, U. V.: Are noctilucent clouds truly a miner's canary of global change?, *EOS T. Am. Geophys. Un.*, 84, 261–268, 2003.